ORIGINAL ARTICLE

EEG dynamic source imaging using a regularized optimization with spatio-temporal constraints

Mayadeh Kouti[1,2] · Karim Ansari-Asl[1] · Ehsan Namjoo[1]

Abstract

One of the most important needs in neuroimaging is brain dynamic source imaging with high spatial and temporal resolution. EEG source imaging estimates the underlying sources from EEG recordings, which provides enhanced spatial resolution with intrinsically high temporal resolution. To ensure identifiability in the underdetermined source reconstruction problem, constraints on EEG sources are essential. This paper introduces a novel method for estimating source activities based on spatio-temporal constraints and a dynamic source imaging algorithm. The method enhances time resolution by incorporating temporal evolution of neural activity into a regularization function. Additionally, two spatial regularization constraints based on L_1 and L_2 norms are applied in the transformed domain to address both focal and spread neural activities, achieved through spatial gradient and Laplacian transform. Performance evaluation, conducted quantitatively using synthetic datasets, discusses the influence of parameters such as source extent, number of sources, correlation level, and SNR level on temporal and spatial metrics. Results demonstrate that the proposed method provides superior spatial and temporal reconstructions compared to state-of-the-art inverse solutions including STRAPS, sLORETA, SBL, dSPM, and MxNE. This improvement is attributed to the simultaneous integration of transformed spatial and temporal constraints. When applied to a real auditory ERP dataset, our algorithm accurately reconstructs brain source time series and locations, effectively identifying the origins of auditory evoked potentials. In conclusion, our proposed method with spatio-temporal constraints outperforms the state-of-the-art algorithms in estimating source distribution and time courses.

Keywords EEG source imaging · Non-stationary neural activity · Spatio-temporal constraints · Regularization

1 Introduction

The electroencephalography (EEG) is a suitable noninvasive approach to investigate electrophysiological mechanisms with high temporal resolution [1–4]. EEG signals are primarily generated by synchronized activation of pyramidal neurons on the cortex, but due to volume conduction effects, direct interpretation of EEG measurements is challenging [5, 6]. EEG source imaging methods have evolved to enhance spatial specificity by projecting sensor signals to neural activity, improving interpretability [7, 8]. However, with the limited number of electrodes compared to the multitude of neural sources, the inverse problem becomes ill-posed. To address this, regularization techniques with a priori constraints are applied to narrow the solution space and obtain optimal solutions [9–30].

Classical methods like minimum-norm estimates (MNE) minimize source power using L_2-norm, but they tend to estimate superficial sources more frequently [9]. To mitigate this issue, Weighted MNE (WMNE) weights the regularization term using the columns' norm of the lead field matrix, penalizing superficial sources more than deep ones [31, 32]. In LOw REsolution TomogrAphy (LORETA), a discrete Laplacian operator (the second-order spatial derivatives of sources) is used as the weighting matrix, resulting in

✉ Karim Ansari-Asl
karim.ansari@scu.ac.ir; karim.ansari@gmail.com

Mayadeh Kouti
m.kouti@scu.ac.ir

Ehsan Namjoo
ehsan.namjoo@scu.ac.ir

1   Department of Electrical Engineering, Faculty of Engineering, Shahid Chamran University of Ahvaz, Ahvaz, Iran

2   Department of Electrical Engineering, Shohadaye Hoveizeh Campus of Technology, Shahid Chamran University of Ahvaz, Ahvaz, Iran

improved spatial smoothness [10]. sLORETA standardizes source reconstruction by using source variance, enhancing robustness against superficial sources and noise [12]. Statistical Parameter Mapping (dSPM) is another linear source estimation technique similar to the aforementioned methods, providing a noise-normalized minimum-norm estimate at a given source location [33]. It is calculated by dividing the activity estimate at each source location by the baseline standard deviation of the noise.

Although the approaches based on L_2-norm are appropriate for reconstructing distributed sources [1], they yield spread solutions for sparse sources. L_1-norm methods, inspired by sparse signal processing, avoid overfitting and accurately estimate focal sources [17]. However, sparseness regularizers may fail to determine the spatial extent of distributed sources, leading to scattered estimation [1]. To address this issue, a transformed version of sources using methods like spatial gradient or wavelet transform can be used to induce sparsity [20, 34–38]. For example, in [34], the "Variation-Based Sparse Cortical Current Distribution (VB-SCCD)" method was introduced to locate EEG/MEG inverse solutions by penalizing source gradients. This approach employs a variation transform to compute differences between adjacent grid dipoles.

Existing methods in EEG source imaging primarily focus on spatial regularity of sources, overlooking temporal evolution, which contains valuable information for improving source reconstruction. However, these methods often apply separate estimations at each time sample, leading to noise-sensitive and non-smooth results. Incorporating temporal information into inverse solvers enhances understanding of source dynamics and stabilizes solutions [39, 40]. Various techniques aim to improve source estimation by considering temporal aspects [29, 40–55], such as applying temporal regularization terms or formulating dynamic inverse problems [41, 42, 45, 56, 57]. The authors of [40, 43, 44, 46, 58–61] formulate the dynamic inverse problem using a state estimation problem and evince the spatio-temporal constraints as a part of the system equation. For example, a random walk model with spatial Laplacian constraints is employed to show the dynamics of EEG sources [43, 44], or in STRAPS method a nearest-neighbor multivariate autoregressive (MVAR) model is utilized to formulate the spatio-temporal connections [60]. Another approach is mixed-norm estimation, which integrates spatio-temporal regularization ($L_{1,2}$-norm) to achieve spatially sparse solutions with temporally smooth recovery using temporal basis functions [29, 50–54].

In this work, an iterative regularized algorithm in a transformed domain based on spatio-temporal constraints is proposed. The proposed method (PM) can be considered an extension of the algorithm proposed in [62] that uses spatial basis decomposition and spatio-temporal constraints. The principal contribution of this paper is the insertion of one temporal constraint and two transformed spatial constraints considering physiological facts of sources. It offers two variants: the first variant deals with extended sources while the second variant deals with focal sources. In the proposed method, temporal variations of sources are modeled using a random walk model, and temporal smoothness is imposed using an L_2-norm of a time-domain differencing operator. In the next step, two spatial constraints are proposed for spread and focal sources. The first spatial constraint utilizes L_2-norm and the Laplacian operator to exploit spatial clustering of neuronal activity (PM-L_2) [63]. This idea comes from the fact that adjacent neural populations have more probability of showing synchronous activity [64] due to mutual interactions among brain areas, indicating spatially clustered neuronal activity [65]. The second spatial constraint employs an L_1-norm and variational transformation to impose sparsity, particularly suitable for estimating focal sources (PM-L_1) [34]. This approach stems from the physiological observation that activated brain regions are concentrated rather than distributed across the entire cortical surface. To prevent over-focused solutions, the variational transform delineates boundaries between inactive and active cortical regions, promoting sparseness. The performance of the proposed method is evaluated using both simulated data and real EEG recordings from auditory ERP experiments. Quantitative assessment, conducted with synthetic datasets, investigates the effects of parameters such as source extent, number of sources, correlation level, and SNR level on temporal and spatial metrics. Our results demonstrate that our dynamic method with the proposed spatio-temporal constraints outperforms state-of-the-art algorithms in estimating source distribution and time courses.

2 Materials and methods

To describe EEG signals, a linear model Eq. (1) is used as follows:

$$y_t = Gx_t + \varepsilon_t \tag{1}$$

where y_t is scalp EEG measurements vector, G stands for the lead field matrix that correlates the sources inside the brain and sensor recordings, x_t is the vector of cortical sources (defined in terms of current dipoles), and ε_t is the measurement noise. Here, y_t is an $M \times 1$ vector, where M denotes the number of electrodes; G is an $M \times N$ matrix, where N shows the number of sources; x_t is a vector of $N \times 1$, and ε_t is an $M \times 1$ vector with spatial covariance $Q_\varepsilon \in \mathbb{R}^{M \times M}$.

2.1 Inverse problem framework

The constrained regularization model for reconstructing current sources Eq. (2) is formulated as:

$$\underset{x_t}{\text{minimize}} \ \|y_t - Gx_t\|^2_{2,Q_\varepsilon}$$

Subject to $\|\Gamma x_t\|^l_l = 0$ (2)

$$\|x_t - \hat{x}_{t-1}\|^2_{2,Q_\eta} = 0$$

where $\hat{x}_t$ denotes the estimate of x_t at time instant t, Γ denotes the transformation matrix, and $\|.\|^l_{l,\Pi}$ denotes the l norm weighted by Π (e.g., in the case of $l = 2$ $\|a - b\|^2_{2,\Pi} = (a - b)^T \Pi^{-1}(a - b)$). The first term of Eq. (2) measures the difference between the observed EEG signals and their estimates from estimated sources.

Based on a priori knowledge, we introduce additional constraints to the cortical sources. In addressing the dynamic inverse problem, we incorporate spatio-temporal constraints grounded in neurophysiological facts. As previously mentioned, we impose two types of spatial constraints. The conventional hypothesis posits that sources are distributed, which can be incorporated into the inverse solution by applying the Laplacian matrix to the cortical surfaces [63]. Consequently, the transformed sources are constrained to minimize energy using the L_2-norm.

The second spatial constraint focuses on the sparsity of sources, relevant in cases of focal epilepsy or ERP activities [28]. This constraint is incorporated by utilizing the variation matrix (gradient of underlying sources) [34]. So, in lieu of L_2-norm, we apply the L_1-norm to reconstruct the spatio-temporal dynamics of sparse cortical sources. Additionally, to prevent extremely focal solutions, the variation matrix is employed to derive sparse spatial representation. Both constraints are formulated as a transformation matrix (Γ) in Eq. (2).

To enhance the temporal smoothness of the reconstructed sources, we introduce the last term in Eq. (2) as a temporal constraint, utilizing the L_2-norm of a time-domain differencing operator. To consider the dynamics of sources, x_t is modeled as a random walk model, e.g., $x_t = x_{t-1} + \eta_t$. In this model, the source vector x_t at time t is a linear combination of its past value. We assume process noise with covariance $Q_\eta \in \mathbb{R}^{N \times N}$ to account for unknown factors influencing the evolution of cortical sources.

2.2 Estimation cortical sources using a dynamic regularization with spatio-temporal constraints

In this work, we employ Tikhonov regularization, known for its effectiveness in addressing dynamic inverse problems. At $t = 1$, an initial estimation of the current sources x_1 can be found using any inverse problem method, e.g., MNE. Subsequently, optimization problems are solved iteratively for each time instant from $t = 2, 3, ..., T$. Estimates of the current sources x_t can be achieved by iteratively through a regularized algorithm. The approach for dynamic inverse problem solutions is described in Eq. (3):

$$\hat{x}_t = \underset{x_t}{\text{argmin}}\{F_l(x_t, \gamma_t, \lambda_t)\} = \underset{x_t}{\text{argmin}}\{\|y_t - Gx_t\|^2_{2,Q_\varepsilon} + \gamma_t\|\Gamma x_t\|^l_l + \lambda_t\|x_t - \hat{x}_{t-1}\|^2_{2,Q_\eta}\} \quad (3)$$

Here, γ_t and λ_t represent the regularization parameters utilized to minimize the penalty function and the sources residual norm weighted by their variances, respectively. The trade-off between these parameters significantly influences the optimization task.

For smooth distribution, interactions between neighboring voxels are considered by incorporating the Laplacian matrix. This helps alleviate the biasing issues commonly associated with L_2-norm solutions. The Laplacian matrix consists of the second-order spatial derivatives, as defined in Eq. (4):

$$L_{i,j} = \begin{cases} 1 & i = j \\ -\frac{1}{\sqrt{d_i d_j}} & (i,j) \in \mathcal{E} \\ 0 & Otherwise \end{cases} \quad (4)$$

where $L_{i,j}$ indicates the entry at the i-th row and j-th column of matrix $L \in \mathbb{R}^{N \times N}$; d_i and d_j show the number of neighbors of the i-th and j-th sources, respectively. Also, $\mathcal{E}$ indicates the edges set of the cortical model [63].

Therefore, the neural activity estimation is achieved by minimizing the cost function described in Eq. (5):

$$F_l(x_t, \gamma_t, \lambda_t) = \|y_t - Gx_t\|^2_{2,Q_\varepsilon} + \gamma_t\|x_t\|^2_{2,W} + \lambda_t\|x_t - \hat{x}_{t-1}\|^2_{2,Q_\eta} \quad (5)$$

where $W = (L^T L)^{-1}$.

In the case of sparse sources, L_2-norm solutions result in undesirable and unrealistic results. These smooth solutions tend to reconstruct spatially blurred sources that spread across extensive brain regions, resulting in ghost sources. To address this, we employ the L_1-norm instead of L_2-norm to estimate the spatio-temporal dynamics of sparse sources. However, the drawback of the L_1-norm is that it drives the optimization problem towards extremely focal solutions. To achieve sparsity in a different domain, we use a transformation matrix to penalize a gradient version of the underlying sources. This is accomplished using the variation transform matrix, as discussed in [34]. The variation matrix, denoted as V, captures amplitude differences between adjacent dipoles. In cases where sources are distributed almost uniformly, notable differences often occur at the edges of activated and inactivated regions [66], manifesting as sparse features [34]. The variation matrix is substituted into the second term of Eq. (3) to enforce sparsity on the cortical sources, as defined in Eq. (6):

$$F_l(x_t, \gamma_t, \lambda_t) = \|y_t - Gx_t\|^2_{2,Q_\varepsilon} + \gamma_t\|V x_t\|^1_1 + \lambda_t\|x_t - \hat{x}_{t-1}\|^2_{2,Q_\eta} \quad (6)$$

The elements $v_{e,n}$ of V ($e = 1, \dots, E, n = 1, \dots, N$) are defined as follows: E is the number of triangular edges and N is the number of the triangles in the cortical current Eq. (7) distribution model

$$v_{e,n} = \begin{cases} 1 & if n = n_{e,1} \\ -1 & if n = n_{e,2} \\ 0 & otherwise \end{cases} \qquad (7)$$

where $n_{e,1}$ and $n_{e,2}$ show the indices of the source diploes that shares the e-th edge. Besides, the definition of matrix V can be extended to models that the sources are positioned at the grid vertices. To obtain a closed-form analytical solution of Eq. (6), the L_1-norm can be approximated according to [67] as given in Eq. (8).

$$\|Vx_t\|_1 \approx \|Vx_t\|_{2,Q}^2 \qquad (8)$$

where $Q = diag(|\hat{x}_{t-1}|), Q \in \mathbb{R}^{N \times N}$. We have a similar form of the cost function for the L_1-norm, with the different W matrix. Here, W matrix is defined as $W^{-1} = V^T Q^{-1} V$.

Furthermore, the matrices of covariance are supposed to be the identity for simplicity ($Q_\varepsilon = I_M$ and $Q_\eta = I_N$). The Jacobian of Eq. (6) with respect to x_t results in Eq. (9):

$$\begin{aligned}\frac{\partial F_t}{\partial x_t} &= -G^T y_t + G^T G x_t + \gamma_t W^{-1} x_t + \lambda_t x_t - \lambda_t \hat{x}_{t-1} \\ &= -WG^T y_t + WG^T G x_t + \gamma_t x_t + \lambda_t W x_t - \lambda_t W \hat{x}_{t-1}\end{aligned} \qquad (9)$$

By setting Eq. (9) equal to zero, $\hat{x}_t$ is derived Eq. (10) as follows [62]:

$$\hat{x}_t = \left(WG^T G + \gamma_t I_N + \lambda_t W\right)^{-1} W(G^T y_t + \lambda_t \hat{x}_{t-1}) \qquad (10)$$

In the subsequent step, it is crucial to objectively select appropriate values for the hyper-parameters γ_t and λ_t since the solution is highly dependent on these parameters. Different approaches, like the L-curve [68] and the generalized cross-validation (GCV) [69, 70], have been employed for hyper-parameter selection. Here, we estimate hyper-parameter values using the GCV method by minimizing the cost function defined in Eq. (11):

$$v(\gamma_t, \lambda_t) = \frac{\|Gx_t(\gamma_t, \lambda_t) - y_t\|_2^2}{tr(I_M - GG^\dagger(\gamma_t, \lambda_t))^2} \qquad (11)$$

Here, the notation $tr(.)$ indicates the trace of the argument matrix, and G represents the regularized inverse of the lead field matrix $G^\dagger$ defined as Eq. (12):

$$G^\dagger = (WG^T G + \gamma_t I_N + \lambda_t W)^{-1} WG^T \qquad (12)$$

We conduct several simulations to assess the performance of the proposed method. The reconstructed solutions are compared with the ground truth and their differences are computed using several metrics. Furthermore, we compare both proposed algorithms (PM-L_1 and PM-L_2) against some state-of-the-art methods such as STRAP, sLORETA, dSPM, MxNE, and SBL. The validation encompasses changes in SNR levels, spatial source extends, the number of active sources, and the coupling strength between sources.

2.3 EEG data simulation

To simulate the EEG recordings, patch sources are considered on the cortical surface. These source signals generate time series of alpha oscillations (8–13 Hz) and have a 3-s length with a sampling frequency of 250 Hz. We examine three scenarios concerning spatial patch extents, the number of active dipoles, and the coupling strength between sources. Patches are generated by selecting one, three, and five active sources (seeds) with random locations on the cortex. Each active dipole corresponds to a patch on the cortical surface, constructed by growing a region around the selected dipole. To probe the performance of the inverse problem approach, we vary the source sizes to achieve both sparse and smooth distributions.

In the real world, activity distribution is smooth because of the synchronization of neighboring neurons [71]. Therefore, we employ a three-dimensional Gaussian-shaped power distribution to smooth the source amplitudes within the patches and prevent abrupt power level changes. Sources orientations are assumed to be fixed and perpendicular to the cortex [5, 13]. The geodesic distance between nodes of the cortical mesh serves as the distance metric. The spatial standard deviation of the amplitude distributions is 10 mm for a small spatial extent and 34 mm for a large spatial extent.

To develop more accurate simulations, both measurement and biological noises are incorporated. The biological noise is modeled as the power spectral density inversely proportional to the frequency (denoted as pink or flicker noise). Specifically, we add additional Gaussian noise with $\frac{1}{f}$ spectral density at a signal-to-noise ratio (SNR) of 10 dB to account for background brain activity to 1000 randomly selected dipoles for each trial. An example of the simulated signals for three simulated sources is depicted in Online Resource 1.

In the next step, the forward problem is solved by calculating the lead field matrix. The cortex model is derived from the ICBM152 template anatomy (an MRI atlas) [72–74]. The lead field matrix is obtained using a boundary element model (BEM) [75]. This model contains brain, skull, and skin layers with 0.33 S/m, 0.0165 S/m, and 0.33 S/m conductivities, respectively [72, 76]. For the forward model, a coarse mesh with 8000 nodes and a mean distance of 5 mm between neighboring vertices is employed. The brain activity of cortical sources is mapped to sensor space using source activity and lead

field matrices to generate EEG signals with 128 electrodes according to the standard BIOSEMI-128 electrodes configuration. Additionally, Gaussian noises with varying variance values are added as measurement noise. Each testing set holds 50 trials for every scenario. The simulation codes are implemented in MATLAB (Mathworks Inc., MA, USA), incorporating functions from Brainstorm [77] and FieldTrip [78] toolboxes.

2.4 Real EEG database

The real EEG dataset is from an auditory odd-ball experiment studied in [79]. While the dataset includes data from 12 participants, we only use data from ten healthy subjects with normal hearing, who are non-smokers, and aged between 21 and 34. Participants were requested to count target stimuli and ignore non-target ones during the online spelling task experiment. 63-channel EEG signals were acquired using wet Ag/AgCl electrodes placed symmetrically based on the international 10–20 system.

On average, each experiment consists of 120 trials with target stimuli and 450 trials with non-target stimuli. Each stimulus has 100 ms latency and the inter-stimulus onset interval is 225 ms. The channels are referenced to the nose. The original sampling frequency is 1 kHz, but to reduce the computational load of the data analysis, the EEG recordings were down-sampled to 250 Hz. In the pre-processing step, a fifth-order Butterworth filter is used to filter the EEG signals between 0.4 and 25 Hz. The data is epoched between -150 and 800 ms relative to the stimulus onset, with a baseline correction from -150 to 0 ms. For source imaging, the epochs are averaged across each condition. The same lead field matrix is generated using FieldTrip toolbox based on a 5-mm resolution (8000 vertices) BEM model.

2.5 Performance measures

To evaluate the performance of the proposed method in both temporal and spatial domains, we employ multiple quantitative validation metrics as described below:

2.5.1 Spatial accuracy index

Earth-Movers Distance Earth-Movers Distance (EMD) denoted by $m_{emd} \in \mathbb{R}^+$ compares the spatial distribution of the dipole-wise estimated sources power with simulated ones [36]. The EMD provides an appropriate measure for quantifying dissimilarity between two activity distributions and is defined as:

$$m_{emd} = d_e \left\{ X_e, \hat{X}_e \right\} \tag{13}$$

where $X_e \epsilon \mathbb{R}^{N \times 1}$ is the simulated activity energy averaged over time and $\hat{X}_e$ is its estimate. Thus, a lower value of m_e indicates better reconstruction quality.

Spatial dispersion Spatial dispersion (SD) is a measure to evaluate the extent to which the sources are spatially blurred [80]. A low SD value is desired for an imaging approach, and it is defined as:

$$m_{sd} = \sqrt{\frac{\sum\limits_{n=1}^{N} \sum\limits_{i \in I_n} d_{ni}^2 \|\hat{x}_i\|_2^2}{\sum\limits_{i}^{d_s} \|\hat{x}_i\|_2^2}} \tag{14}$$
$$I_n = \left\{ i \mid n = argmin_{n\prime} d_{n\prime i} \right\}, 1 < n\prime < N$$

where $\hat{x}_i$ denotes the ith row of the reconstructed sources $\hat{X}$, d_{ni} shows the distance between simulated source n and the sources i, and N is the number of the sources. I_n denotes the set of indices of sources in the reconstruction map to which the n th source is the closest. The minimum distance is zero when the source i belongs to I_n. Spatial dispersion values near zero indicate no active source outside the simulated patch, while large values may result from spurious sources or spatial spread of the estimated source around the original source extent.

2.5.2 Temporal accuracy index

Variance explained Temporal accuracy index, $m_{ve} \in \mathbb{R}[0, 1]$, measures the value of Variance Explained (VE) obtained from the channel recordings using reconstructed sources, defined as follows:

$$m_{ve} = 1 - \frac{\|G\hat{X} - Y\|_2^2}{\|Y - \overline{Y}\|_2^2} \tag{15}$$

where $\hat{X} \epsilon \mathbb{R}^{N \times T}$ represents the reconstructed activity of distributed sources and matrix $\overline{Y} \epsilon \mathbb{R}^{M \times T}$ contains the temporal average of all channels.

Correlation Correlation, denoted by $m_c \in \mathbb{R}[0, 1]$, measures the strength and the direction of a linear relationship between the estimated source time series and the ground truth. A higher correlation value indicates higher accuracy in estimating the source time series.

2.5.3 Statistics

We assess the statistical difference in precision to determine if our proposed method outperforms other methods. We employ a two-sample *t*-test for this purpose, where the null hypothesis suggests no significant differences between our method and others based on the mean values of the evaluation measures. In contrast, the alternative hypothesis indicates that our mean values are lower/higher (depends on the evaluation measures) than the average values achieved by other methods (p-value < 0.05 uncorrected).

3 Results and discussion

3.1 Results of simulated data

We examined two primary aspects of the inverse solution's performance: spatial and temporal resolution. For this purpose, we tested simulated data exhibiting non-stationary behavior and varying source amplitudes across different spatial extents, source numbers, SNR levels, and interaction scenarios. It is important to highlight that our proposed method offers two versions: one tailored for extended sources (PM-L_2) and another for focal sources

(PM-L_1). Reconstructions results are compared to state-of-the-art inverse solutions including STRAPS [60], sLORETA [12], SBL [15], dSPM [33], and MxNE [51].

3.2 One active patch source with different spatial extents

We evaluated the performance of various methods using a single active patch source with both small and large spatial extents. The first elements of Figs. 1 and 2 show the simulated sources with small and large spatial extents, respectively, along with their corresponding reconstruction maps. For the small active region, PM-L_1, MxNE, SBL, and STRAPS provide solutions with high fidelity (Fig. 1). Notably, STRAPS and MxNE are flexible in simultaneously estimating the location and extent of the active source, while SBL shows ability in sparse source reconstruction. However, SBL tends to enforce sparsity in the original source space leading to overly focused estimation, especially for extended sources. As previously mentioned, PM-L_1 enforces sparsity in the variation domain of sources. Using this transformed spatial domain and temporal constraint makes PM-L_1 achieve better performance in the source localization. On the other hand, PM-L_2, dSPM, and sLORETA yield over-diffused estimates due to their preference for spatially blurred solutions. Figure 1 shows that none of aforementioned methods can
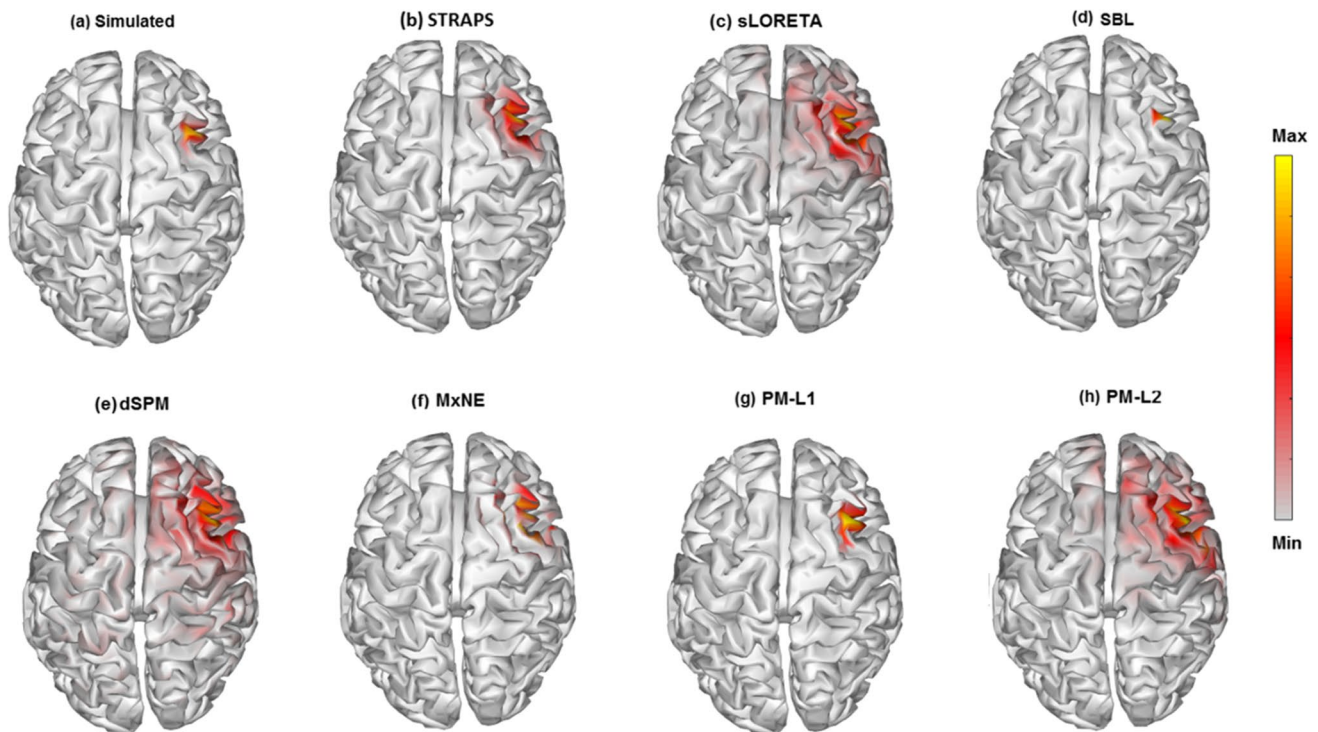

Fig. 1 Simulated small active patch and its reconstructions. (a) The simulated active region. The maps (b) to (h) demonstrate the localization of the reconstructed activity in the alpha band (8–13 Hz) with 15 dB SNR using STRAP, sLORETA, SBL, dSPM, MxNE, PM-L_1, and PM-L_2, respectively

accurately identify focal sources without spatial leakage. They yield the worst results for focal simulated data due to their non-sparse nature. Additionally, it can be seen that dSPM produces some scattered activations as false active sources.

For large active sources, STRAPS provides estimates that closely resembles the ground truth (Fig. 2). While STRAPS has no prior assumption about sources and is flexible in recovering location and extent, our results indicate that it struggles to accurately recover the extent of extended sources. In contrast, MxNE offers a more focal estimation compared to STRAPS. On the other hand, due to the enforced sparsity on the original source domain, SBL obtains a highly focal estimate compared to the origin active region. Although PM-L_1 is a sparse constrained method, it does not produce very focal estimation as it employs the variation transform of sources and offers a better reconstruction of source extent. Finally, the L_2-norm methods (e.g., sLORETA, dSPM, and PM-L_2) estimations match better with the ground truth. Among the aforementioned methods, we can see that PM-L_2 yields estimate that closely match the ground truth. PM-L_2 provides a smoother response due to the use of Laplacian transformation. Using this smoothing spatial constraint as well as the temporal constraint makes its reconstruction more accurate than other approaches.

Figure 3 shows the mean and standard deviation (S.D.) values of the quantitative evaluators (EMD, VE, spatial dispersion, and correlation) for each method. In this test, a

single patch source is simulated in two sizes (small: 10 mm and large: 34 mm) with a 15 dB SNR. The reconstruction results are based on 50 trials. In the case of the small patch source, L_1-norm methods (e.g., PM-L_1, SBL, MxNE) and STRAPS outperform L_2 regularization methods in spatial source reconstruction. L_2-norm methods (e.g., PM-L_2, dSPM, and sLORETA) are less sensitive to the extent of sources, leading to over-diffused estimations with large EMD and spatial dispersion values. This finding corroborates the visual analysis from Fig. 1, demonstrating an over-estimation of the spatial extent and the presence of several spurious sources around the true patch in L_2-based methods. Among the methods, PM-L_1 performs best across all evaluation metrics, with significantly lower EMD values compared to sLORETA, dSPM, SBL, and PM-L_2 ($p < 0.01$). Furthermore, the EMD values of PM-L_1 are significantly smaller than the spatio-temporal solvers, e.g., STRAP and MxNE ($p < 0.05$). Moreover, for the spatial dispersion metric, it shows significantly the best performance ($p < 0.01$).

In the case of the large patch source, PM-L_2 demonstrates significantly better spatial performance across all evaluators ($p < 0.05$), while it leads to a blurred reconstruction and low spatial accuracy for focal patch sources. SBL struggles with reconstructing large patch sources but performs better as the source size decreases. Figure 3 also presents temporal evaluation for all the solvers. Since the proposed method (L_1 and L_2), MxNE and STRAPS solutions include temporal penalty term, they outperform SBL, dSPM, and sLORETA
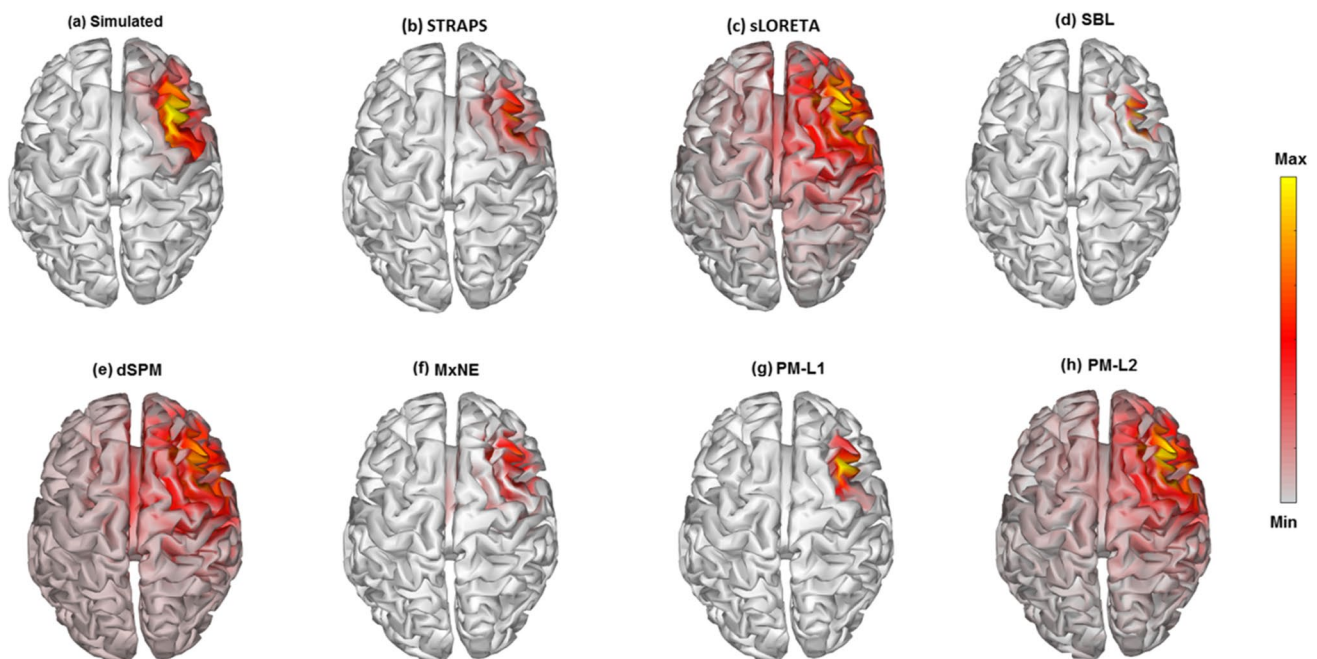

Fig. 2 Simulated large active patch and its reconstructions. (a) The simulated active region. The maps (b) to (h) demonstrate the localization of the reconstructed activity in the alpha band (8–13 Hz) with 15 dB SNR, using STRAP, sLORETA, SBL, dSPM, MxNE, PM-L_1, and PM-L_2, respectively

Fig. 3 Spatial and temporal performance (mean ± SD) using STRAP, sLORETA, SBL, dSPM, MxNE, PM-L_1, and PM-L_2, respectively. Results of one active patch reconstruction are computed using 50 realizations for each simulated small and large patch sources randomly placed on the cortex when SNR is 15 dB. Generated EEGs include non-stationary temporal dynamics in the alpha band (8–13 Hz)
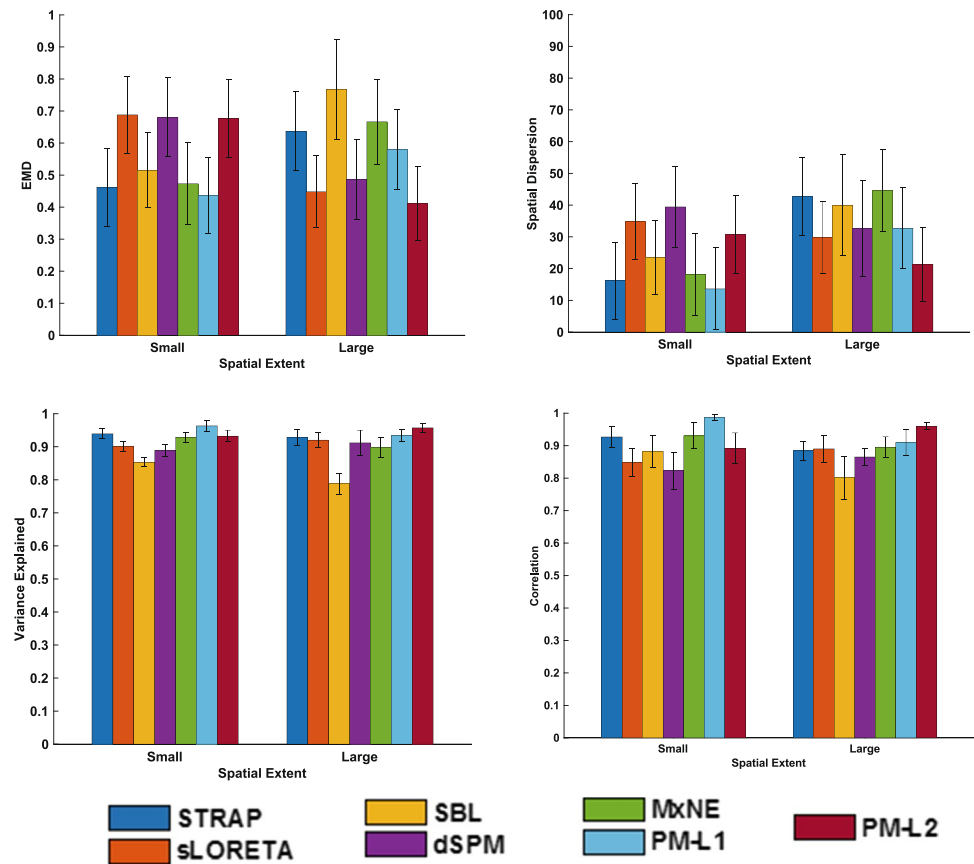
in recovering the dynamics of the simulated data regardless of the spatial extent. It can be seen that for the large patch source, PM-L_2 demonstrates significantly higher VE and correlation values compared to the other methods, while for the small patch source, PM-L_1 shows significantly the best VE and correlation results ($p < 0.05$).

3.2.1 Simulation results of multiple active patch sources

In this analysis, we consider different numbers of patch sources (one, three, and five) with small spatial extent. The spatial and temporal reconstruction performances of all methods for different numbers of sources are quantified by the validation metrics over varying SNR values (-5, 0, 5, 10, 15 dB) as presented in Fig. 4 and 5, respectively. Regarding spatial evaluation, it can be observed that PM-L_1, STRAPS, MxNE, and SBL achieve more accurate source recovery, as indicated by their lower EMD values for all numbers of active sources and SNRs (left columns of Fig. 4). Additionally, Fig. 4 demonstrates that all L_2 minimum-norm solutions, e.g., sLORETA, dSPM, and PM-L_2, exhibit similar characteristics, resulting in overly blurry reconstructions that cover a large portion of the cortices with poor spatial accuracy, as indicated by larger EMD values. This observation aligns with the visual analysis from Fig. 1, which shows an overestimation of

spatial extent by dSPM and sLORETA. Specifically, dSPM generates scattered sources and sLORETA yields spatially blurred solutions. Statistically, PM-L_1 exhibits significantly lower EMD values than sLORETA, dSPM, SBL, and PM-L_2 ($p < 0.01$). Comparing the spatio-temporal solvers, PM-L_1 also demonstrates smaller EMD values than STRAP and MxNE, across the tested SNRs ($p < 0.05$).

However, for three sources at 5 dB SNR, PM-L_1 shows a numerically lower EMD value than STRAP without significance (PM-L_1:0.509 ± 0.118, STRAP:0.519 ± 0.106, $p = 0.208$). When it comes to spatial dispersion, it can be observed that PM-L_1 achieves the smallest spatial dispersion value significantly ($p < 0.01$). This finding is validated by Fig. 1, which demonstrates PM-L_1 as the most accurate solver in identifying the spatial extent of the small sources. Additionally, PM-L_1 exhibits the most robustness towards noise and consistently provides the best performance for spatial dispersion across all tested SNRs. Among the methods, spatial dispersion values of dSPM and sLORETA are large, which is noted earlier by Hauk et al. [81] that sLORETA and dSPM are more similar to each other. It worth noting that MxNE, which utilizes $L_{1,2}$ norm penalization, outperforms L_2-norm regularization methods such as sLORETA, dSPM, or PM-L_2 in reconstructing sources. Moreover, SBL solution is focal and displays small spatial dispersion due to

Fig. 4 Spatial reconstruction accuracy (EMD and spatial dispersion (mean ± SD)) of multiple active patches using STRAP, sLORETA, SBL, dSPM, MxNE, PM-L_1, and PM-L_2. Results are computed after 50 realizations for each simulated activity of one, three, and five sparse sources randomly located on the cortex with various SNR levels (−5, 0, 5, 10, and 15). Generated EEGs include non-stationary temporal dynamics in the alpha band (8–13 Hz)
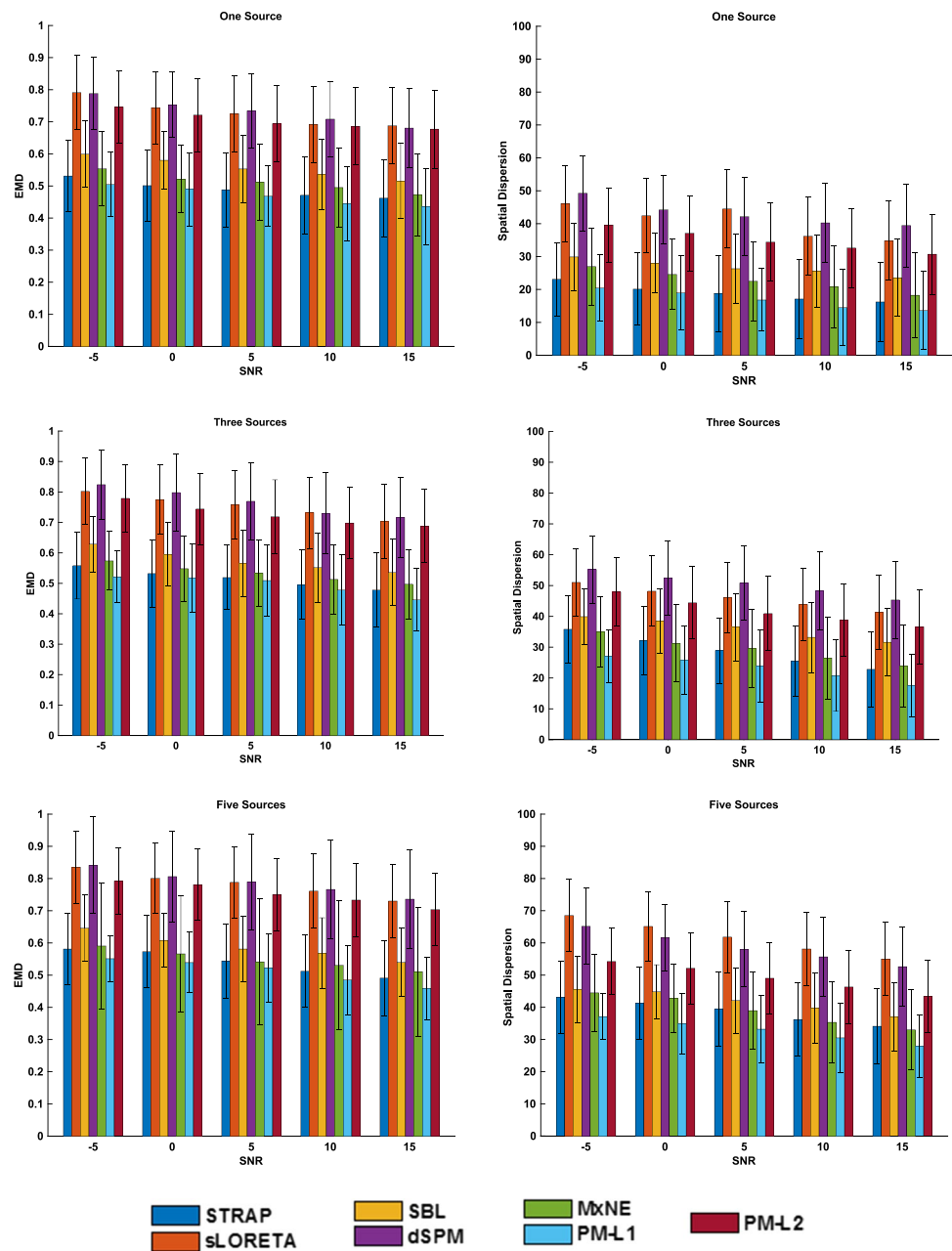

the sparsity constraint, as evidenced by the small EMD and spatial dispersion values. Furthermore, an increase in the number of active sources and noise level leads to a decrease in EMD and spatial dispersion values. Figure 4 also underscores the merit of PM-L_1 as it demonstrates less sensitive to the number of sources and SNR levels.

Concerning temporal accuracy, we observe that the noise level is a critical parameter for all the methods, as lower SNRs lead to lower performances (Fig. 5). It can be realized that the increasing number of active sources results in decreased temporal metrics values. Our findings indicate that the proposed approach (L_1 and L_2) is less sensitive to the number of sources and

noise levels in comparison to other exiting methods. Specifically, sLORETA, dSPM, and SBL exhibit lower temporal accuracy as they lack temporal information. Conversely, it is observed that the proposed method (L_1 and L_2) as well as STRAPS and MxNE demonstrate less time error due to the inclusion of temporal constraint in their solving algorithm. These results reveal that the non-stationarity in temporal dynamics of the simulated data has a primary effect on the performance of algorithms. PM-L_2 achieves an appropriate temporal pattern, even though its spatial extent does not exactly resemble the simulated one (blurred estimated source). STRAPS and MxNE exhibit better performance than PM-L_2 in terms of

Fig. 5 Temporal reconstruction accuracy (EV and correlation (mean ± SD)) of multiple active patches using STRAP, sLORETA, SBL, dSPM, MxNE, PM-L_1, and PM-L_2. Results are computed after 50 realizations for each simulated activity of one, three, and five sparse sources randomly located on the cortex with various SNR levels (− 5, 0, 5, 10, and 15). Generated EEGs include non-stationary temporal dynamics in the alpha band (8–13 Hz)
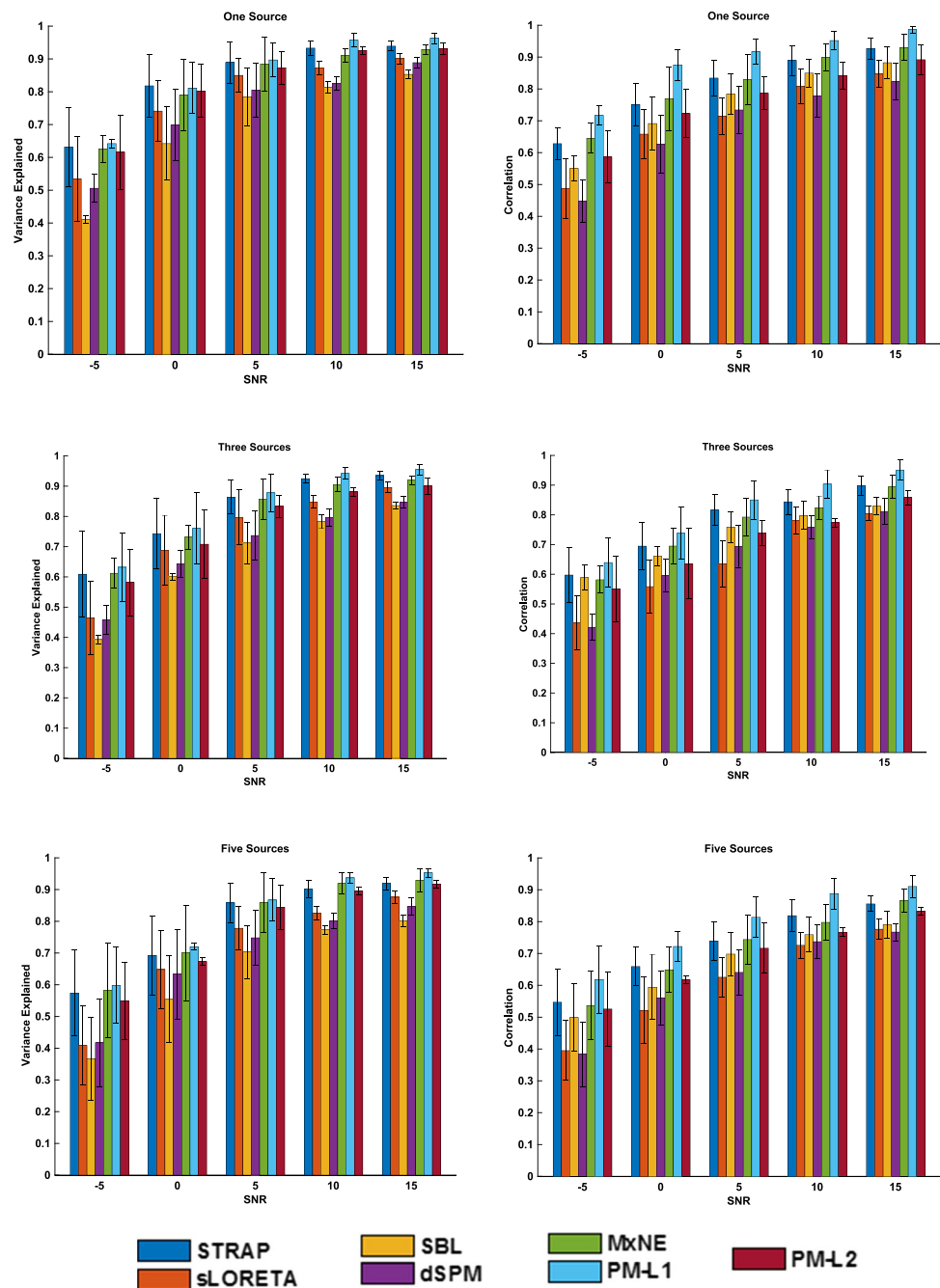
both spatial and temporal metrics, as they are based on a spatio-temporal constraint and designed to reconstruct sparse sources. We also assessed the CPU runtimes that are required for the application of the proposed imaging method. To measure the execution times and run the algorithms, a computer with 3.7 GHz Intel Core i7 processor and 16 GB of RAM was used. For one-patch scenario, the average runtimes are 355.8 ± 2.7s and 382.6 ± 1.4 s for PM-L_1 and PM-L_2, respectively. In addition, when the

activated sources are increased, the execution time for the proposed methods slightly increases.

Finally, in this case (small sources), PM-L_1 significantly achieves the best reconstruction performance in terms of VE and correlation evaluators among the exiting methods ($p < 0.05$) under all SNRs and numbers of sources. The dynamic model of the proposed method, which incorporates temporal evolution, leads to enhanced temporal source recovery. This temporal insight not only enhances the method's temporal accuracy but also enriches the spatial reconstruction of underlying neural sources.

Furthermore, by customizing the regularization terms, our algorithm demonstrates versatility in addressing both focal and distributed source reconstructions.

3.2.2 Influence of correlated sources on reconstruction results

Interaction between source time series in different active regions is challenging for source reconstruction. Therefore, we assess the impact of interaction between the time series of two active sources. For this purpose, we simulate two scenarios: one with interacting and another with non-interacting distributed (large) patch sources. In Fig. 6, we compute the spatial and temporal metrics for the compared methods in both scenarios. It can be seen that the interaction between sources leads to a decrease in the performance of all the methods. According to Fig. 6, PM-L_2 method yields significantly lowest EMD values ($p < 0.05$), followed by sLORETA and dSPM. Additionally, PM-L_2 consistently exhibits significantly robust performance with lower spatial dispersion for both interacted and non-interacted sources ($p < 0.01$).

Regarding the temporal reconstruction evaluation, it is observed that PM methods (both L_1 and L_2) demonstrate less sensitivity to the interaction between two active sources. This is due to the simultaneous use of spatial and temporal constraints, resulting in lower temporal error. As shown in Fig. 6, PM-L_2 achieves significantly higher VE and correlation values compared to other existing methods in both interacted and non-interacted scenarios ($p < 0.05$).

3.3 Results of auditory ERP dataset

The auditory ERP dataset was utilized to assess the proposed technique's real-world performance. For the purpose of visual perception, Fig. 7 and Fig. 8 display the proposed method source reconstruction for non-target and target stimuli, respectively. Both figures depict estimated scalp topographies based on the sensor space data, epoch-averaged time series, dipole-wise source power, and the most powerful sources time series reconstructed by PM-L_1 and PM-L_2, respectively. As previously noted, PM-L_1 designed for focal source reconstruction, while PM-L_2 yields extended sources.

In Fig. 7's first subfigure, ERP signals indicate a noticeable peak at around 200 ms after the stimulus onset (marked in a red line). The second subfigure illustrates scalp topography at $t = 180$ ms. Subfigures 7(d) and 7(f) depict the corresponding dipole-wise source power at the same time point using PM-L_1 and PM-L_2, respectively. We choose $t = 180$ ms

Fig. 6 Spatial and temporal reconstruction performances (mean ± SD) of two active patches at different coupling values using STRAP, sLORETA, SBL, dSPM, MxNE, PM-L_1, and PM-L_2. Results are computed using 50 realizations for each simulated activity of two distributed sources randomly located on the cortex. Generated EEGs include non-stationary temporal dynamics in the alpha band (8–13) Hz with different coupling values. The SNR is 15 dB in these cases
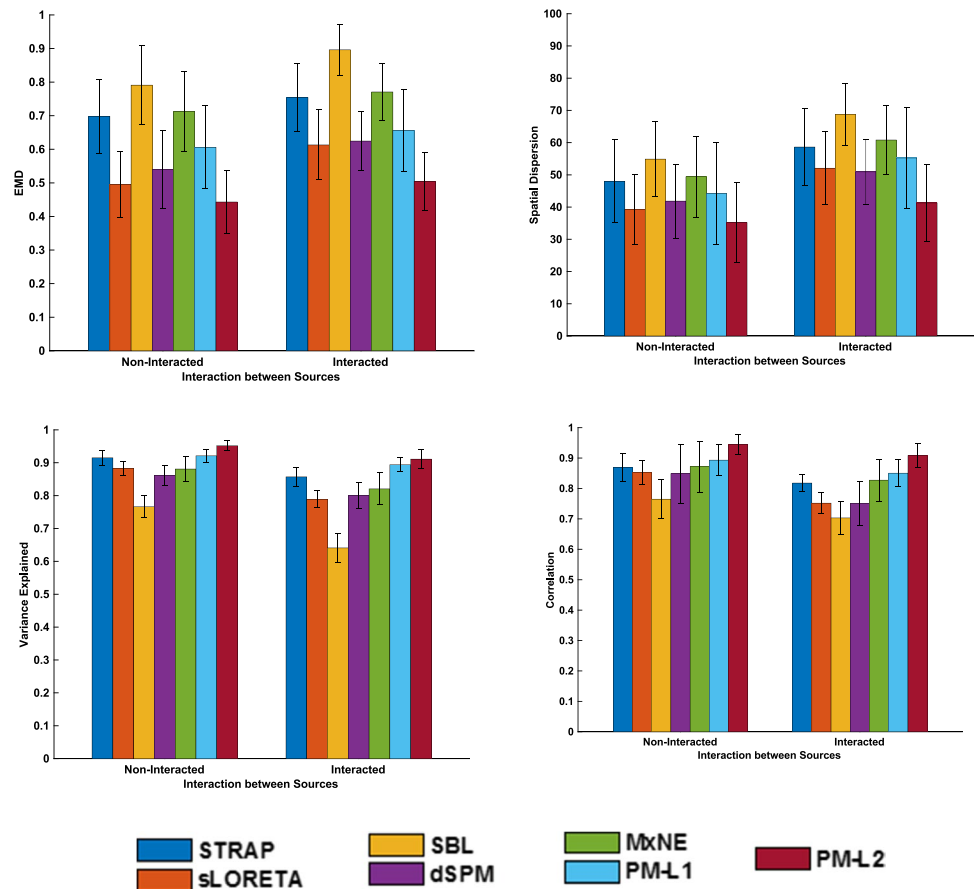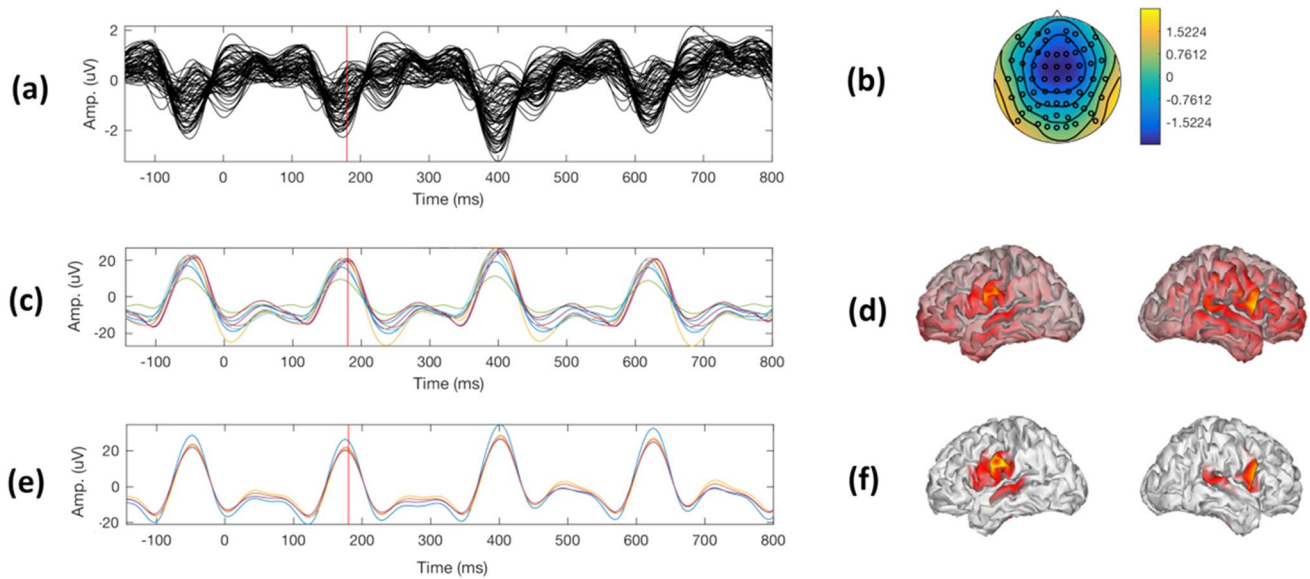
Fig. 7 The proposed method reconstruction results for non-target stimuli of subject 6. (a) Time series of the averaged trials and the time point $t = 0$ ms indicates the beginning of stimulus. The red vertical line at $t = 180$ ms displays the N180 component. (b) Scalp maps computed for the averaged trials. Subfigures 7(d) and 7(f) The reconstructed source power achieved by PM-L_1 and PM-L_2 at $t = 180$ ms indicated with a vertical line in the top plot. Subfigures 7(c) and 7(e) Time series of the most significant sources reconstructed by PM-L_1 and PM-L_2, respectively
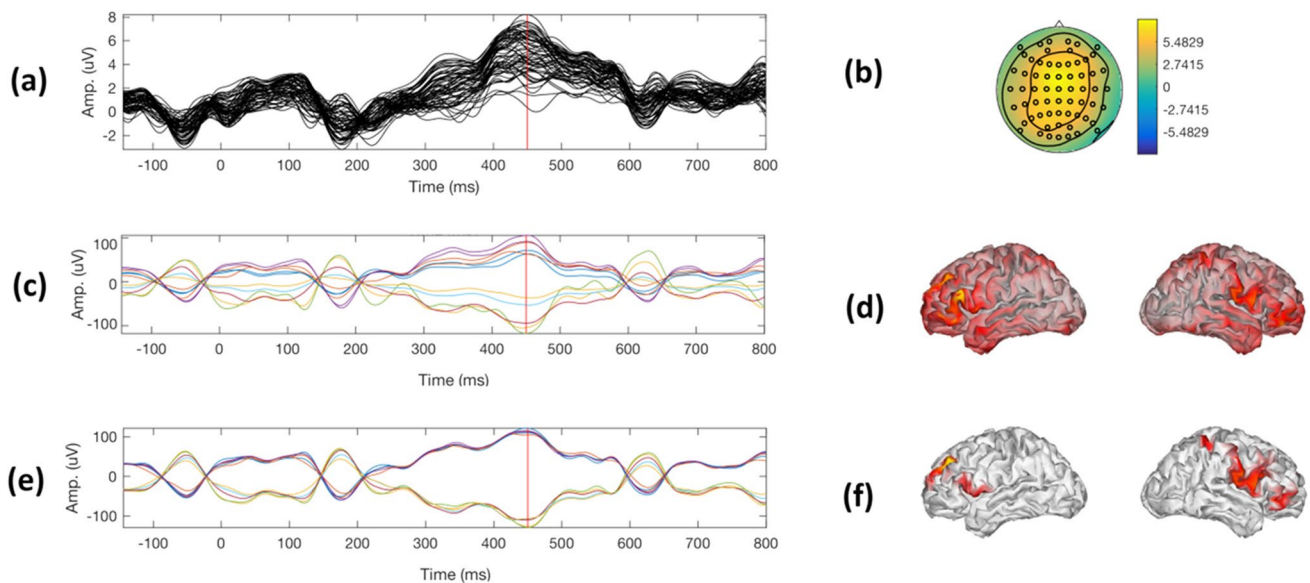

Fig. 8 The proposed method reconstruction results for target stimuli response of subject 6. (a) Time series of the averaged trials and the time point $t = 0$ ms indicates the beginning of stimulus. The red vertical line at $t = 450$ ms shows the P3 component. (b) Scalp maps computed for the averaged trials. Subfigures 8(d) and 8(f) The reconstructed source power achieved by PM-L_1 and PM-L_2 at $t = 450$ ms indicated with a vertical line in the top plot. Subfigures 8(c) and 8(e) Time series of the most significant sources reconstructed by PM-L_1 and PM-L_2, respectively

to show the N180 component, which includes specific brain responses associated with auditory processing [79]. The results highlight activity located surrounding the auditory cortex, namely, the superior temporal gyrus and lateral sulcus, which has been associated with the structural encoding of auditory [82–84]. Subfigures 7(c) and 7(e) present the time series of the primary sources reconstructed by PM-L_1 and PM-L_2, respectively. These time series exhibit a clean representation of the original ERP dynamics associated with

the N180 ERP component, with periodic peaks reflecting the stimulus interval every 225 ms.

For target stimuli, subfigure 8(a) shows the averaged trial time series with a notable peak around 450 ms post-stimulus onset (highlighted by a red line). Subfigure 8(b) displays the estimated scalp from ERP data at $t = 450$ ms. Subfigures 8(d) and 8(f) show the corresponding dipole-wise source power at this time point reconstructed by PM-L_1 and PM-L_2, respectively. We selected $t = 450$ ms to show the P3 ERP component, including specific brain responses associated with the auditory processing [79]. It can be seen that the activity in the auditory cortex decreases compared to non-target stimuli, with heightened activity in central and frontal regions, possibly indicating increased conscious processing [53]. Subfigures 8(c) and 8(e) depict the estimated time courses of the most powerful sources reconstructed by PM-L_1 and PM-L_2, respectively. It can be seen a noticeable peak around 450 ms, possibly correlates with the P3 ERP component [79]. It is worth mentioning that the results from all subjects matched the quality of those selected for visualization.

To sum up, our algorithm effectively reconstructs realistic brain sources by integrating spatio-temporal constraints to enhance both temporal and spatial accuracy. Furthermore, through customized regularization terms, our algorithm showcases versatility in addressing both focal and distributed source reconstructions, as notably demonstrated in auditory evoked potentials. Peaks corresponding to auditory and perception areas are distinctly visible. Non-target stimuli predominantly activate regions around the auditory cortex, like the superior temporal gyri. In contrast, target stimuli also show increased activity in central and frontal regions, indicative of conscious stimulus processing. These findings align with prior studies on auditory ERP source locations [82–84]. For both types of stimuli, PM-L_2 provides dispersed estimates, while PM-L_1 gives more focused results due to its sparsity constraint on the transformed source domain. Temporally, source signals correspond to various perception stages, highlighting the algorithm's ability to capture neural processes.

We also applied our proposed method to a high-resolution EEG dataset collected during an emotion study (for more details, refer to Online Resource 2). Incorporating spatial smoothness and sparsity, along with temporal smoothness, yielded effective performance in our experiments. These results are consistent with previous research, providing insights into the locations of activated brain regions associated with both positive and negative emotions [85–90]. Additionally, we explored the impact of electrode numbers on the accuracy of active region identification, using four standard electrode configurations ranging from 32 to 257 electrodes. The findings revealed that employing more electrodes enhances the localization of active regions.

Furthermore, we observed significant differences in brain responses between positive and negative stimuli.

As a limitation of our study, we employed a generic three-compartment BEM head model to solve the forward problem in brain source estimation. This approach introduces inaccuracies by using a template MRI rather than individualized neuroanatomy, which lacks important geometric information for each subject and omits cerebrospinal fluid (CSF) in the model. These limitations can lead to imprecise transformation of EEG sensor data into a template cortical manifold that deviates from the real one. To improve future research, we plan to employ a more comprehensive 4- or 5-compartment head model that includes CSF and considers skull anisotropy through finite element modeling. Additionally, in subsequent studies, we aim to validate our approach using data from epilepsy surgery and incorporate a more sophisticated model of brain activity to capture cortical dynamics more accurately, thereby refining our inverse problem solution.

4 Conclusions

In this study, we introduced a novel EEG source imaging method that leverages spatio-temporal constraints for both distributed and focal sources inspired by underlying neurophysiological principles. Our approach combines temporal smoothness with spatial constraints based on both L_1 and L_2 norm regularization terms, utilizing spatial gradient and Laplacian transforms of sources to enhance spatial resolution. The method's uniqueness lies in its dynamic model that integrates temporal evolution, leading to improved temporal source recovery. This temporal insight not only elevates the method's temporal accuracy but also enriches the spatial reconstruction of underlying neural sources. Moreover, by tailoring the regularization terms, our algorithm exhibits versatility in addressing both focal and distributed source reconstructions. Through extensive simulations, we demonstrated the method's superiority over five state-of-the-art algorithms: STRAPS, sLORETA, SBL, dSPM, and MxNE. The proposed algorithm consistently outperformed these methods in spatial and temporal source reconstruction. We evaluated the proposed method in a real-world application involving auditory evoked potentials and HR-EEG emotional states. As a result, the proposed approach shows a strong capability in recovering neural brain activity and localizing major areas for both auditory and emotional states. In conclusion, our method offers a promising advancement in EEG source imaging, emphasizing the integration of spatio-temporal constraints to enhance both temporal and spatial accuracy. The results underscore its potential in effectively recovering brain activity and identifying major brain regions

across various scenarios, further validating its relevance in advancing neuroimaging research.

Declarations

Conflict of interest The authors declare no competing interests.

References

1. He B, Yang L, Wilke C, Yuan H (2011) Electrophysiological imaging of brain activity and connectivity—challenges and opportunities. IEEE Trans Biomed Eng 58:1918–1931
2. Schölvinck ML, Leopold DA, Brookes MJ, Khader PH (2013) The contribution of electrophysiology to functional connectivity mapping. Neuroimage 80:297–306
3. Kouti M, Ansari-Asl K, Namjoo E (2019) Epileptic source connectivity analysis based on estimating of dynamic time series of regions of interest. Netw Comput Neural Syst 30:1–30
4. Eom T-H (2023) Electroencephalography source localization. Clin Exp Pediatr 66:201
5. Nunez PL, Srinivasan R, Westdorp AF, Wijesinghe RS, Tucker DM, Silberstein RB et al (1997) EEG coherency: I: statistics, reference electrode, volume conduction, Laplacians, cortical imaging, and interpretation at multiple scales. Electroencephalogr Clin Neurophysiol 103:499–515
6. Hallez H, Vanrumste B, Grech R, Muscat J, De Clercq W, Vergult A et al (2007) Review on solving the forward problem in EEG source analysis. J Neuroeng Reheb 4:46
7. Michel C M, Brunet D (2019) EEG source imaging: a practical review of the analysis steps. Front Neurol 10. https://doi.org/10.3389/fneur.2019.00325
8. Asadzadeh S, Rezaii TY, Beheshti S, Delpak A, Meshgini S (2020) A systematic review of EEG source localization techniques and their applications on diagnosis of brain abnormalities. J Neurosci Method 339:108740
9. Hämäläinen MS, Ilmoniemi RJ (1994) Interpreting magnetic fields of the brain: minimum norm estimates. Med Biol Eng Comput 32:35–42
10. Pascual-Marqui RD, Michel CM, Lehmann D (1994) Low resolution electromagnetic tomography: a new method for localizing electrical activity in the brain. Int J Psychophysiol 18:49–65
11. Pascual-Marqui RD, Lehmann D, Koenig T, Kochi K, Merlo MC, Hell D et al (1999) Low resolution brain electromagnetic tomography (LORETA) functional imaging in acute, neuroleptic-naive, first-episode, productive schizophrenia. Psychiatry Res Neuroimaging 90:169–179
12. Pascual-Marqui RD (2002) Standardized low-resolution brain electromagnetic tomography (sLORETA): technical details. Methods Find Exp Clin Pharmacol 24:5–12
13. Baillet S, Mosher JC, Leahy RM (2001) Electromagnetic brain mapping. Signal Process Mag IEEE 18:14–30
14. Friston K, Harrison L, Daunizeau J, Kiebel S, Phillips C, Trujillo-Barreto N et al (2008) Multiple sparse priors for the M/EEG inverse problem. Neuroimage 39:1104–1120
15. Wipf D, Nagarajan S (2009) A unified Bayesian framework for MEG/EEG source imaging. Neuroimage 44:947–966
16. He B, Sohrabpour A, Brown E, Liu Z (2018) Electrophysiological source imaging: a noninvasive window to brain dynamics. Annu Rev Biomed Eng 20:171–196
17. Ding L, He B (2008) Sparse source imaging in electroencephalography with accurate field modeling. Hum Brain Mapp 29:1053–1067
18. Gramfort A, Strohmeier D, Haueisen J, Hämäläinen MS, Kowalski M (2013) Time-frequency mixed-norm estimates: sparse M/EEG imaging with non-stationary source activations. Neuroimage 70:410–422
19. Ojeda A, Kreutz-Delgado K, Mullen T (2018) Fast and robust Block-Sparse Bayesian learning for EEG source imaging. Neuroimage 174:449–462
20. Sohrabpour A, Lu Y, Worrell G, He B (2016) Imaging brain source extent from EEG/MEG by means of an iteratively reweighted edge sparsity minimization (IRES) strategy. Neuroimage 142:27–42
21. Martínez-Vargas JD, Duque-Muñoz L, Vargas-Bonilla F, López JD, Castellanos-Dominguez G (2019) Enhanced data covariance estimation using weighted combination of multiple Gaussian kernels for improved M/EEG source localization. Int J Neural Syst 29:1950001
22. Bore JC, Yi C, Li P, Li F, Harmah DJ, Si Y et al (2018) Sparse EEG source localization using LAPPS: least absolute l-P (0< p< 1) penalized solution. IEEE Trans Biomed Eng 66:1927–1939
23. Hamid L, Habboush N, Stern P, Japaridze N, Aydin Ü, Wolters CH et al (2021) Source imaging of deep-brain activity using the regional spatiotemporal Kalman filter. Comput Methods Programs Biomed 200:105830
24. Oliaiee A, Sardouie SH, Shamsollahi MB (2021) Ensemble multi-modal brain source localization using theory of evidence. Biomed Signal Process Control 69:102668
25. Kouti M, Ansari-Asl K, Namjoo E (2022) Emotion discrimination using source connectivity analysis based on dynamic ROI identification. Biomed Signal Process Control 72:103332
26. Hirata A, Niitsu M, Phang CR, Kodera S, Kida T, Rashed EA et al (2024) High-resolution EEG source localization in personalized segmentation-free head model with multi-dipole fitting. Phys Med Biol 69:055013
27. Liu K, Wang Z, Yu Z, Xiao B, Yu H, Wu W (2023) WRA-MTSI: a robust extended source imaging algorithm based on multi-trial EEG. IEEE Trans Biomed Eng 70:2809–2821
28. Becker H, Albera L, Comon P, Gribonval R, Wendling F, Merlet I (2015) Brain-source imaging: from sparse to tensor models. IEEE Signal Process Mag 32:100–112
29. Becker H, Albera L, Comon P, Nunes J-C, Gribonval R, Fleureau J et al (2017) SISSY: an efficient and automatic algorithm for the analysis of EEG sources based on structured sparsity. Neuroimage 157:157–172
30. Liu K, Yu ZL, Wu W, Gu Z, Li Y (2020) Imaging brain extended sources from EEG/MEG based on variation sparsity using automatic relevance determination. Neurocomputing 389:132–145
31. Dale AM, Sereno MI (1993) Improved localizadon of cortical activity by combining EEG and MEG with MRI cortical surface reconstruction: a linear approach. J Cogn Neurosci 5:162–176
32. Eddy M, Schmid A, Holcomb PJ (2006) Masked repetition priming and event-related brain potentials: a new approach for tracking the time-course of object perception. Psychophysiology 43:564–568
33. Dale AM, Liu AK, Fischl BR, Buckner RL, Belliveau JW, Lewine JD et al (2000) Dynamic statistical parametric mapping:

combining fMRI and MEG for high-resolution imaging of cortical activity. Neuron 26:55–67

34. Ding L (2009) Reconstructing cortical current density by exploring sparseness in the transform domain. Phys Med Biol 54:2683

35. Liao K, Zhu M, Ding L (2013) A new wavelet transform to sparsely represent cortical current densities for EEG/MEG inverse problems. Comput Methods Programs Biomed 111:376–388

36. Haufe S, Nikulin VV, Ziehe A, Müller K-R, Nolte G (2008) Combining sparsity and rotational invariance in EEG/MEG source reconstruction. Neuroimage 42:726–738

37. Zhu M, Zhang W, Dickens DL, Ding L (2014) Reconstructing spatially extended brain sources via enforcing multiple transform sparseness. Neuroimage 86:280–293

38. Chang W-T, Nummenmaa A, Hsieh J-C, Lin F-H (2010) Spatially sparse source cluster modeling by compressive neuromagnetic tomography. Neuroimage 53:146–160

39. Scherg M (1990) Fundamentals of dipole source potential analysis. Auditory evoked magnetic fields and electric potentials. Adv Audiol 6:40–69

40. Zhang Y, Ghodrati A, Brooks DH (2005) An analytical comparison of three spatio-temporal regularization methods for dynamic linear inverse problems in a common statistical framework. Inverse Probl 21:357

41. Brooks DH, Ahmad GF, MacLeod RS, Maratos GM (1999) Inverse electrocardiography by simultaneous imposition of multiple constraints. IEEE Trans Biomed Eng 46:3–18

42. Schmitt U, Louis AK, Darvas F, Buchner H, Fuchs M (2001) Numerical aspects of spatio-temporal current density reconstruction from EEG-/MEG-data. IEEE Trans Med Imaging 20:314–324

43. Yamashita O, Galka A, Ozaki T, Biscay R, Valdes-Sosa P (2004) Recursive penalized least squares solution for dynamical inverse problems of EEG generation. Hum Brain Mapp 21:221–235

44. Galka A, Yamashita O, Ozaki T, Biscay R, Valdés-Sosa P (2004) A solution to the dynamical inverse problem of EEG generation using spatiotemporal Kalman filtering. Neuroimage 23:435–453

45. Schmitt U, Louis A (2002) Efficient algorithms for the regularization of dynamic inverse problems: I. Theory Inverse Probl 18:645

46. Lamus C, Long CJ, Hamalainen MS, Brown EN, Purdon PL (2007) Parameter estimation and dynamic source localization for the magnetoencephalography (MEG) inverse problem. 2007 4th IEEE International Symposium on Biomedical Imaging: From Nano to Macro, Arlington, VA, USA, pp 1092–1095. https://doi.org/10.1109/ISBI.2007.357046

47. Limpiti T, Van Veen BD, Attias HT, Nagarajan SS (2009) A spatiotemporal framework for estimating trial-to-trial amplitude variation in event-related MEG/EEG. IEEE Trans Biomed Eng 56:633–645

48. Daunizeau J, Mattout J, Clonda D, Goulard B, Benali H, Lina J-M (2006) Bayesian spatio-temporal approach for EEG source reconstruction: conciliating ECD and distributed models. IEEE Trans Biomed Eng 53:503–516

49. Bolstad A, Van Veen B, Nowak R (2009) Space–time event sparse penalization for magneto-/electroencephalography. Neuroimage 46:1066–1081

50. Ou W, Hämäläinen MS, Golland P (2009) A distributed spatio-temporal EEG/MEG inverse solver. Neuroimage 44:932–946

51. Gramfort A, Kowalski M, Hämäläinen M (2012) Mixed-norm estimates for the M/EEG inverse problem using accelerated gradient methods. Phys Med Biol 57:1937

52. Strohmeier D, Bekhti Y, Haueisen J, Gramfort A (2016) The iterative reweighted mixed-norm estimate for spatio-temporal MEG/EEG source reconstruction. IEEE Trans Med imaging 35:2218–2228

53. Castaño-Candamil S, Höhne J, Martínez-Vargas J-D, An X-W, Castellanos-Domínguez G, Haufe S (2015) Solving the EEG inverse problem based on space–time–frequency structured sparsity constraints. Neuroimage 118:598–612

54. Montoya-Martínez J, Artés-Rodríguez A, Hansen L K, Pontil M (2012) Structured sparsity regularization approach to the EEG inverse problem. 2012 3rd International workshop on cognitive information processing (CIP), Baiona, Spain, pp 1–6. https://doi.org/10.1109/CIP.2012.6232898

55. Trujillo-Barreto NJ, Aubert-Vázquez E, Penny WD (2008) Bayesian M/EEG source reconstruction with spatio-temporal priors. Neuroimage 39:318–335

56. Schmitt U, Louis AK, Wolters C, Vauhkonen M (2002) Efficient algorithms for the regularization of dynamic inverse problems: II. Applications Inverse Probl 18:659

57. Zhou H, Wang Y, Li Y, Ruan D, Liu W (2018) Improving EEG source localization with a novel regularization: spatiotemporal graph total variation (STGTV) method. 2018 40th Annual International conference of the ieee engineering in medicine and biology society (EMBC), Honolulu, HI, USA, pp 4673–4676. https://doi.org/10.1109/EMBC.2018.8513128

58. Lamus C, Hämäläinen MS, Temereanca S, Brown EN, Purdon PL (2012) A spatiotemporal dynamic distributed solution to the MEG inverse problem. Neuroimage 63:894–909

59. Pirondini E, Babadi B, Obregon-Henao G, Lamus C, Malik WQ, Hämäläinen MS et al (2018) Computationally efficient algorithms for sparse, dynamic solutions to the EEG source localization problem. IEEE Trans Biomed Eng 65:1359–1372

60. Liu K, Yu ZL, Wu W, Gu Z, Li Y (2015) Straps: a fully data-driven spatio-temporally regularized algorithm for M/EEG patch source imaging. Int J Neural Syst 25:1550016

61. Long CJ, Purdon PL, Temereanca S, Desai NU, Hämäläinen MS, Brown EN (2011) State-space solutions to the dynamic magnetoencephalography inverse problem using high performance computing. Ann Appl Stat 5:1207

62. Giraldo-Suarez E, Martínez-Vargas JD, Castellanos-Dominguez G (2016) Reconstruction of neural activity from EEG data using dynamic spatiotemporal constraints. Int J Neural Syst 26:1650026

63. Bradshaw L, Wikswo J (2001) Spatial filter approach for evaluation of the surface Laplacian of the electroencephalogram and magnetoencephalogram. Ann Biomed Eng 29:202–213

64. Engel C, Hamilton JD (1990) Long swings in the dollar: are they in the data and do markets know it? Am Econ Rev 80:689–713

65. Mesulam M (1990) Large-scale neurocognitive networks and distributed processing for attention, language, and memory. Ann Neurol 28:597–613

66. Cottereau B, Jerbi K, Baillet S (2007) Multiresolution imaging of MEG cortical sources using an explicit piecewise model. Neuroimage 38:439–451

67. Fan J, Li R (2001) Variable selection via nonconcave penalized likelihood and its oracle properties. J Amer Statist Assoc 96:1348–1360

68. Hansen BE (1994) Autoregressive conditional density estimation. Int Econ Rev 1:705–730

69. Grech R, Cassar T, Muscat J, Camilleri KP, Fabri SG, Zervakis M et al (2008) Review on solving the inverse problem in EEG source analysis. J Neuroeng Rehab 5:25

70. Wahba G (1990) Spline models for observational data. Siam 59:153–169. https://doi.org/10.1137/1.9781611970128

71. Haalman I, Vaadia E (1997) Dynamics of neuronal interactions: relation to behavior, firing rates, and distance between neurons. Hum Brain Mapp 5:249–253

72. Oostendorp TF, Delbeke J, Stegeman DF (2000) The conductivity of the human skull: results of in vivo and in vitro measurements. IEEE Trans Biomed Eng 47:1487–1492

73. Zhang Y, Van Drongelen W, He B (2006) Estimation of in vivo brain-to-skull conductivity ratio in humans. Appl Phys Lett 89:223903

74. Mazziotta JC, Toga AW, Evans A, Fox P, Lancaster J (1995) A probabilistic atlas of the human brain: theory and rationale for its development. The International Consortium for Brain Mapping (ICBM). Neuroimage 2:89–101

75. Mosher JC, Leahy RM, Lewis PS (1999) EEG and MEG: forward solutions for inverse methods. IEEE Trans Biomed Eng 46:245–259

76. Lai Y, Van Drongelen W, Ding L, Hecox K, Towle V, Frim D et al (2005) Estimation of in vivo human brain-to-skull conductivity ratio from simultaneous extra-and intra-cranial electrical potential recordings. Clin Neurophysiol 116:456–465

77. Tadel F, Baillet S, Mosher JC, Pantazis D, Leahy RM (2011) Brainstorm: a user-friendly application for MEG/EEG analysis. Comput Intell Neurosci 2011:879716

78. Oostenveld R, Fries P, Maris E, Schoffelen J-M (2011) FieldTrip: open source software for advanced analysis of MEG, EEG, and invasive electrophysiological data. Comput Intell Neurosci 2011:156869

79. Höhne J, Schreuder M, Blankertz B, Tangermann M (2011) A novel 9-class auditory ERP paradigm driving a predictive text entry system. Front Neurosci 5:99

80. Molins A, Stufflebeam SM, Brown EN, Hämäläinen MS (2008) Quantification of the benefit from integrating MEG and EEG data in minimum ℓ2-norm estimation. Neuroimage 42:1069–1077

81. Hauk O, Wakeman DG, Henson R (2011) Comparison of noise-normalized minimum norm estimates for MEG analysis using multiple resolution metrics. Neuroimage 54:1966–1974

82. Rusiniak M, Lewandowska M, Wolak T, Pluta A, Milner R, Ganc M et al (2013) A modified oddball paradigm for investigation of neural correlates of attention: a simultaneous ERP–fMRI study. Magn Reson Mater Phys Biol Med 26:511–526

83. Justen C, Herbert C (2018) The spatio-temporal dynamics of deviance and target detection in the passive and active auditory oddball paradigm: sLORETA study. BMC Neurosci 19:1–18

84. Ragazzoni A, Di Russo F, Fabbri S, Pesaresi I, Di Rollo A, Perri RL et al (2019) "Hit the missing stimulus". A simultaneous EEG-fMRI study to localize the generators of endogenous ERPs in an omitted target paradigm. Sci Rep 9:1–15

85. Keil A, Bradley MM, Hauk O, Rockstroh B, Elbert T, Lang PJ (2002) Large-scale neural correlates of affective picture processing. Psychophysiology 39:641–649

86. Koelsch S, Fritz T, v Cramon DY, Müller K, Friederici AD (2006) Investigating emotion with music: an fMRI study. Hum Brain Mapp 27:239–250

87. Keuper K, Zwanzger P, Nordt M, Eden A, Laeger I, Zwitserlood P et al (2014) How 'love'and 'hate'differ from 'sleep': using combined electro/magnetoencephalographic data to reveal the sources of early cortical responses to emotional words. Hum Brain Mapp 35:875–888

88. Padilla-Buritica JI, Martinez-Vargas JD, Castellanos-Dominguez G (2016) Emotion discrimination using spatially compact regions of interest extracted from imaging EEG activity. Front Comput Neurosci 10:55

89. Chen G, Zhang X, Sun Y, Zhang J (2020) Emotion feature analysis and recognition based on reconstructed EEG sources. IEEE Access 8:11907–11916

90. Proverbio AM, Cesati F (2024) Neural correlates of recalled sadness, joy, and fear states: a source reconstruction EEG study. Front Psychiatry 15:1357770

Publisher's Note Springer Nature remains neutral with regard to jurisdictional claims in published maps and institutional affiliations.

Mayadeh Kouti was born in Ahvaz, Iran in 1988. She received her B.sc, M.sc, and the Ph.D. degrees in electrical engineering all from Shahid Chamran University of Ahvaz, Ahvaz, Iran, in 2010, 2012, and 2019, respectively. She is currently an Assistant Professor at the Department of Electrical Engineering, Shohadaye Hoveizeh Campus of Technology, Susangerd, Iran. Her research interests include biomedical signal and image processing, brain source imaging, inverse problem, brain networks, and connectivity analysis.

Karim Ansari-Asl received the B.Sc. degree in electronic engineering from Semnan University, Semnan, Iran, in 1995, the M.Sc. degree in biomedical engineering from Iran University of Science and Technology (IUST), Tehran, Iran, in 1999, and the Ph.D. degree in biomedical signal processing from the University of Rennes 1, Rennes, France, in 2005. From 2005 to 2007, he was a Postdoctoral Fellow with the University of Rennes 1 and the University of Geneva. Since 2008, he has been with the Electrical Engineering Department, Shahid Chamran University of Ahvaz, Ahvaz, Iran. His research interests include artificial intelligence, pattern recognition, biomedical engineering, digital signal, and image processing.

Ehsan Namjoo received the B.Sc. degree in Electrical Engineering from the K. N. Toosi University of Technology, Tehran, Iran, in 2004 and his M.Sc. and Ph.D. in Communications from the University of Tabriz, Tabriz, Iran in 2006 and 2011 respectively. Since 2012 he has been a faculty member of Shahid Chamran University of Ahvaz, Ahvaz, Iran. His research interests include Information theory, Machine Learning, and Signal processing.